

UCLA

UCLA Previously Published Works

Title

Ab initio investigations on hydrodynamic phonon transport: From diffusion to convection.

Permalink

<https://escholarship.org/uc/item/3835x98z>

Authors

Wu, Huan

Hu, Yongjie

Publication Date

2024-03-01

DOI

10.1016/j.ijheatmasstransfer.2023.124988

Peer reviewed



Published in final edited form as:

Int J Heat Mass Transf. 2024 March ; 220: . doi:10.1016/j.ijheatmasstransfer.2023.124988.

***Ab initio* investigations on hydrodynamic phonon transport: From diffusion to convection**

Huan Wu, Yongjie Hu*

Department of Mechanical and Aerospace Engineering, University of California, Los Angeles, CA 90095, United States of America

Abstract

In classical theory, heat conduction in solids is regarded as a diffusion process driven by a temperature gradient, whereas fluid transport is understood as convection process involving the bulk motion of the liquid or gas. In the framework of *ab initio* theory, which is directly built upon quantum mechanics without relying on measured parameters or phenomenological models, we observed and investigated the fluid-like convective transport of energy carriers in solid heat conduction. Thermal transport, carried by phonons, is simulated in graphite by solving the Boltzmann transport equation using a Monte Carlo algorithm. To capture convective transport, with phonon distributions deviating significantly from equilibrium Bose-Einstein distribution, we determined phonon interactions using *ab initio* approaches that go beyond relaxation time approximations. The presence of strong momentum-conserved Normal scatterings in graphite introduces a regime for hydrodynamic phonon transport. Fluid-like features, such as vortex and jet flow, are visualized and compared with classical theories on heat diffusion and fluid convection. Our study on phonon convection enhances fundamental understandings of heat conduction in solids from both atomic scale and quantum aspects, innovating thermal designs for future microelectronic devices and other thermal management applications. This potentially offers solutions for heat dissipation challenges in the post-Moore era.

Keywords

Hydrodynamic phonon transport; Monte Carlo simulation; First principles theory

1. Introduction

Convection and diffusion are two basic facets of transport phenomena. Convection involves a collective motion of particles due to external forces, such as pressure differences and gravity, while diffusion stems from the random walk of thermal motions, driving systems

*Corresponding author: yhu@seas.ucla.edu (Y. Hu).

CRedit authorship contribution statement

Huan Wu: Conceptualization, Methodology, Validation, Formal analysis, Investigation, Data curation, Writing – original draft, Visualization. **Yongjie Hu:** Conceptualization, Methodology, Investigation, Resources, Writing – review & editing, Supervision, Project administration, Funding acquisition.

Declaration of Competing Interest

The authors declare that they have no known competing financial interests or personal relationships that could have appeared to influence the work reported in this paper.

with a particle density gradient towards equilibrium. Traditionally, fluid transport has been understood as convection processes involving the bulk motion of molecules in liquid or gas flows [1]. In the classical theory of heat transfer, heat conduction in solids is phenomenologically regarded as a diffusive process, described by Fourier's law; that is, heat flux is proportional to the temperature gradient, but the microscopic picture of such a diffusive process was untouched. With the establishment of quantum theory, the quantization of lattice vibrations introduced the concept of phonons. The lattice vibrations can be considered as the superposition of elementary modes of harmonic waves, and the quantum description of those elementary vibrations is known as a phonon. Microscopically, heat conduction in nonmetals results from phonon transport. Since phonons are quasi-particles, their momentum is not necessarily conserved during phonon-phonon interactions.

The Umklapp scatterings, which destroy momentum, inhibit the collective motion of phonons and impede phonon convection [2]. Consequently, heat transport in solids predominantly exhibits diffusive behavior, which has served as the foundation of the heat transfer theory used across various engineering applications. However, when the phonon-phonon interactions are dominated by momentum-conserved Normal scatterings, a realm for phonon convection—or hydrodynamic phonon transport—emerges. In the hydrodynamic regime, the transport of phonons behaves like fluid. For example, thermal energy can propagate like waves in an ocean, and the resistance to heat flux is dominated by friction with the wall, similar to pipe flow, as described by simplified models [3–8]. In comparison to diffusion, convection can be a more efficient method of heat transfer. Despite their significance in thermal applications, such as heat dissipation in microelectronic devices, the real-space dynamics of phonon hydrodynamic processes have not been thoroughly studied from an *ab initio* perspective.

Ab initio approaches serve as powerful tools for computing phonon transport from first principles without using any measured parameters or phenomenological models. These approaches have been employed to predict materials thermal properties and have achieved good agreement with experiments [9–17]. As for hydrodynamic phonon transport, many studies are based on classical models or partially incorporated with *ab initio* input [3–8]. The Boltzmann transport equation, under Callaway's dual relaxation approximation [18], has been intensively employed to study phonon hydrodynamic transport [5,8], while a comprehensive *ab initio* treatment of phonon interactions beyond the dual relaxation approximation has only been applied to investigate the dynamics of convective phonon transport in steady-state or simple structures [19–21]. Although the Green's function method is based on *ab initio*, it is limited to specific geometries [22]. Recently, the phonon vortex was predicted to exist in graphene by phenomenological models [23] and was later examined by the dual relaxation approximation with *ab initio* determined relaxation time [24]. The dynamics of the phonon vortex have not yet been fully investigated by an *ab initio* approach. Furthermore, theoretical investigations on the phonon vortex so far have been limited to two-dimensional materials, which pose greater challenges for experiments and applications compared to bulk materials.

In this paper, we employ *ab initio* approaches based on density functional theory to simulate the dynamics of hydrodynamic phonon transport in real-space, focusing on a widely used

bulk material, graphite. The three-dimensional mode-resolved phonon Boltzmann transport equation, complemented with *ab initio* phonon interactions that go beyond the relaxation time approximation, is solved using a deviational variance-reduced Monte Carlo algorithm [25–27]. Our simulations reveal anomalous fluid-like behaviors, such as vortex and jet flow, in the heat conduction of graphite, which extend beyond the understanding provided by classical heat transfer theory. Our work broadens the knowledge of heat conduction in solids and provides insights for thermal designs in future microelectronic industries.

2. Method

2.1. Boltzmann transport equation and *ab initio* scattering matrix

The phonon transport process is governed by phonon Boltzmann transport equation (BTE) that describes the dynamics of the phonon distribution function $n_{qs}(x, t)$ as a function of real space x and time t for phonon modes labelled by wavevector \mathbf{q} and polarization s ,

$$\frac{\partial n_{qs}}{\partial t} + \mathbf{v}_{qs} \cdot \nabla n_{qs} = \left(\frac{\partial n_{qs}}{\partial t} \right)_{scatt} \quad (1)$$

where the phonon advection on the left-hand side is balanced by the phonon scatterings on the right-hand side. $\mathbf{v}_{qs} = \partial \omega_{qs} / \partial \mathbf{q}$ is the phonon group velocity, and ω_{qs} is the phonon frequency determined by diagonalizing the dynamic matrix. For diffusive process, the phonon distribution typically remains close to equilibrium, hence the scattering term could be approximated by only considering the distribution deviation of the single mode qs while treating other background modes as equilibrium, which is known as relaxation time approximation. While for hydrodynamic process, the phonon distribution is far away from equilibrium Bose-Einstein distribution due to the collective motion of phonons, so the deviation of all modes should be simultaneously considered using a scattering matrix $\Omega_{qs, q's'}$ that quantifies the transition rates from $q's'$ to qs ,

$$\left(\frac{\partial n_{qs}}{\partial t} \right)_{scatt} = \sum_{\mathbf{q}'s'} \Omega_{qs, q's'} (n_{q's'} - n_{q's'}^0) \quad (2)$$

where n_{qs}^0 is the equilibrium Bose-Einstein distribution function. If only considering the diagonal terms and set the off-diagonal terms of $\Omega_{qs, q's'}$ to zero, Eq. (2) reduces to relaxation time approximation. The scattering matrix is *ab initio* determined by quantum perturbation theory [28] considering three-phonon scattering processes. The details of the methodology to obtain the scattering matrix can be found in our previous work [15]. The only input of this *ab initio* approach is the interatomic force constants, i.e., the expansion coefficients of the interatomic potential with respect to the atomic displacements from equilibrium positions. To get interatomic force constants of graphite, we start with generating an irreducible set of displacement configurations on a supercell with 588 carbon atoms. For each displacement configuration, the interatomic forces were determined from

the electron wave functions derived by density functional theory [15–17,29,30] using Quantum ESPRESSO package [31,32]. Then the interatomic force constants are extracted by fitting the displacement-force set using the ALAMODE package [33]. The cutoff radius of the third-order interatomic force constants is 9 bohr. We used projector-augmented wave pseudopotentials and non-local functional ‘vdW-DF-ob86’ for electron exchange and correlation [34]. The convergence threshold for self-consistency is 10^{-11} . The kinetic energy cutoff for electronic wavefunctions is 120 Ry. The Monkhorst-Pack grids for primitive and supercell are $14 \times 14 \times 6$ and $2 \times 2 \times 2$, respectively. All the parameters for the density functional theory calculations have been carefully checked to make the uncertainty of the forces acting on each atom less than 10^{-6} Ry/bohr. The mesh of the q -points for phonon transport is $50 \times 50 \times 8$.

2.2. Deviational variance-reduced Monte Carlo algorithm

The BTE with full scattering matrix is solved by the recently developed deviational variance-reduced Monte Carlo algorithm [25–27]. The deviational variance-reduced Monte Carlo approach has been demonstrated to quantify phonon transport and provide agreement with experiments in our recent studies [25,26]. In Monte Carlo method, large quantities of sample particles are initialized in real space with assigned phonon modes based on equilibrium Bose-Einstein distribution, and then loop over advection-scattering-sampling procedures to simulate the transport dynamics. In advection procedure, the sample particle moves with group velocity. In scattering procedure, the sample particle changes its mode according to scattering matrix. Temperature and heat flux field are sampled in sampling procedure. Different from conventional Monte Carlo algorithm, our method solves the deviational energy-based Boltzmann transport equation,

$$\frac{\partial \delta f_{q_s}}{\partial t} + \mathbf{v}_{q_s} \cdot \nabla \delta f_{q_s} = \sum_{q' s'} A_{q_s, q' s'} \delta f_{q' s'} \quad (3)$$

where $\delta f_{q_s} = \hbar \omega_{q_s} (n_{q_s} - n_{q_s}^0)$ is the deviational energy of phonon mode q_s , and $A_{q_s, q' s'} = \Omega_{q_s, q' s'} \omega_{q_s} / \omega_{q' s'}$ is the matrix that describes the energy exchange between phonon modes through phonon scatterings. Each sample particle carries a positive or negative unit energy that contributes to the energy deviation from equilibrium distribution. This formalism can provide two benefits: i) The energy can be strictly conserved in scattering procedure by fixing the number of sampling particles. ii) Since the deviation from the equilibrium distribution is much smaller than the distribution itself, sampling the deviation from equilibrium significantly reduces the stochastic uncertainty compared with sampling the distribution function. Based on this deviational variance-reduced Monte Carlo algorithm, the phonon BTE can be efficiently solved.

Another challenging to simulate hydrodynamic process is to deal with the full scattering matrix, which makes our scattering algorithm different from the case under relaxation time approximation [35–38]. Under relaxation time approximation, the scattering probability P_{q_s} under a time interval Δt is determined by relaxation time τ_{q_s} ,

$$P_{qs} = 1 - \exp\left(-\frac{\Delta t}{\tau_{qs}}\right) \quad (4)$$

and Phonons re-distribute to equilibrium after scattering. However, with full scattering matrix, the sample particles change their mode following a probability matrix,

$$P(\Delta t) = e^{A\Delta t} \approx I + A\Delta t \quad (5)$$

where I is identity matrix. And phonons are re-distributed as

$$\delta f_{qs}(t + \Delta t) = \sum_{q's'} P_{qs, q's'}(\Delta t) \delta f_{q's'}(t) \quad (6)$$

The scattering procedure requires more considerations than directly simulated Eq. (6) using a stochastic method, because both $P_{qs, q's'}$ and $\delta f_{q's'}$ can be either positive and negative, and simply flipping the sign of $\delta f_{q's'}$ could break the energy conservation. To account for this complexity, Eq. (6) can be mathematically rewritten as

$$\delta f_{qs}(t + \Delta t) = \sum_{q's'} \text{sgn}[P_{qs, q's'}(\Delta t)] \frac{|P_{qs, q's'}(\Delta t)|}{p_{q's'}} \left[1 + \sum_{n=1}^{\infty} \left(\frac{\bar{p}_{q's'}}{p_{q's'}} \right)^n 2^n \right] \delta f_{q's'}(t) \quad (7)$$

where sgn is the sign function, and

$$p_{q's'} = \sum_{qs} |P_{qs, q's'}| \quad (8a)$$

$$\bar{p}_{q's'} = \sum_{qs} |P_{qs, q's'}| \quad (8b)$$

The Eq. (7) can be implemented through the following algorithm [27]:

For a sample particle at mode j with carried energy ε ,

(1) Transit particle to mode i that satisfies

$$\frac{\sum_{k=1}^{i-1} |P_{k,j}|}{p_j} \leq R < \frac{\sum_{k=1}^i |P_{k,j}|}{p_j} \quad (9)$$

where R is a random variable uniformly distributed in $[0,1)$.

(2) If $P_{i,j} < 0$,

- i. update the energy carried by this sample particle as $\varepsilon' = -\varepsilon$,
- ii. generate two new particles in mode j with carried energy and process each by going to step (1).

Based on this algorithm, the energy conservation can be rigidly enforced in scattering procedure. However, the generation of additional particles can boost up the particle numbers in the simulation domain and generate errors due to out of memory. To solve this problem, a cancellation procedure is arranged after scattering procedure to remove particle pairs that carry opposite energies and are in the same phonon mode and spatial cell.

2.3. Sampling of temperature

In deviational variance-reduced Monte Carlo algorithm, the deviation of the local temperature T away from the background equilibrium temperature T_{eq} , $\Delta T = T - T_{eq}$, is derived from the local deviational energy,

$$\Delta T(x, t) = \frac{\sum_{qs} \delta f_{qs}(x, t)}{C} \quad (10)$$

where C is the volumetric specific heat at T_{eq} .

2.4. Boundary conditions

Three types of boundary conditions can be applied in Monte Carlo simulation, the specular, diffusive, and equilibrium temperature boundary conditions. For specular boundary condition, the sample particles are reflected by the boundary by changing the sign of their velocity component perpendicular to the surface. For diffusive boundary condition, the sample particles that carry deviational energy δf_{qs} randomly change its mode at the boundary according to the distribution of the mode-dependent specific heat C_{qs} , since the deviational energy under the temperature rise ΔT contained by phonon mode qs is $C_{qs}\Delta T$. In a diffusive boundary scattering process, the velocities and the moving directions of the reflected phonons are randomly distributed. At the boundaries maintained at equilibrium temperature, ΔT is fixed at zero, hence the sample particles are removed once arrive at those boundaries.

3. Result and discussion

3.1. Hydrodynamic transport regime

In Fig. 1a, we derive the thermal conductivity of isotopically pure graphite nanowire with diffusive boundary and 4- μm -width square cross-section by solving the BTE through deviational variance-reduced Monte Carlo algorithm. The thermal conductivity of materials can be determined by sampling the heat flux under applied temperature gradient. The temperature gradient is applied by adding a source term to the governing equation,

$$\frac{\partial \delta f_{q_s}}{\partial t} + \mathbf{v}_{q_s} \cdot \nabla \delta f_{q_s} = \sum_{q_{s'}} A_{q_s, q_{s'}} \delta f_{q_{s'}} - C_{q_s} \mathbf{v}_{q_s} \cdot \nabla T \quad (11)$$

where the source term on the right-hand side arises because $f_{q_s}^0$ varies in space when there is a temperature gradient. In our Monte Carlo algorithm, ∇T can emit sample particles that carries deviational energy, leading to non-equilibrium. For the simulation setup, we initialize the sample particles at $x = 0$, $t = 0$, distributed randomly over the cross-section area. The modes are assigned based on the distribution of $|C_{q_s} \mathbf{v}_{q_s} \cdot \nabla T|$ with the sign of the carried unit energy opposite to the sign of $\mathbf{v}_{q_s} \cdot \nabla T$. Then we simulate the evolution of the sample particles and sample the total heat flux as a function of time, yielding the transient heat flux in response to the heating pulse at $t = 0$. We employed a time step of 0.1 ps and used a 20×20 spatial mesh at the nanowire cross-section, which has been confirmed to achieve convergence. In the end, we integrate the responsive heat flux cumulatively over time to determine the steady-state heat flux under ∇T , and derive the thermal conductivity of nanowire. The numerical procedure has been validated by comparing with semi-analytical approximate solutions in Appendix A.

Based on Monte Carlos algorithm, we deterministically recovered the resistance to hydrodynamic heat flux caused by the friction with nanowire wall, analogous to Poiseuille flow in fluids. As shown in Fig. 1a, the calculated thermal conductivity decreases at low and high temperature limit, forming a peak near 100 K. The temperature-dependent thermal conductivity of graphite nanowire can be attributed into three regimes. At low temperature, the phonon mean free path (i.e., the distance a phonon travels between consecutive scatterings) exceeds the nanowire width, causing the phonons to ballistically bounce back and forth between boundaries. In this regime, the thermal conductivity increases with temperature due to the increase of the high energy phonons. At high temperature, thermal energy diffuses along the nanowire, and in this regime, the thermal conductivity drops with increasing temperature due to the increased anharmonic scatterings. In the intermediate hydrodynamic regime, the heat flux flows in the nanowire like Poiseuille flow, and the thermal resistance is partially contributed by the friction with boundary. As shown by the inset of Fig. 1a, the drifting velocity of the collective phonon flux is near zero at the nanowire boundary due to diffusive scattering, increases as it moves away from the boundary, and peaks at the center of nanowire.

3.2. Propagation of hydrodynamic wave packet

To elucidate the transport physics in hydrodynamic regime, the dynamics of the phonon transport in graphite at 100 K is simulated by this *ab initio* approach. Fig. 1b shows the evolution of temperature field response to a given heat pulse at $t = 0$ and $x = 0$. The simulation domain has been made long enough to make sure the propagating phonon density waves do not reach the other boundary. We observed two components of the temperature field, the diffusive and the hydrodynamic component. The two components are extracted by fitting the overall temperature profile with two Gaussian functions. Since the thermal diffusion is driven by phonon density gradient, the diffusive component always has the maximum at the boundary. On the other hand, hydrodynamic component is a propagating wave packet. The temperature field calculated by phonon Boltzmann transport equation exhibits remarkable difference from the solution of the heat diffusion equation,

$$T(x, t) = \frac{1}{\sqrt{4\pi\alpha t}} \exp\left(-\frac{x^2}{4\alpha t}\right) \quad (12)$$

where α is the thermal diffusivity. This contrast showcases the pronounced deviation of the propagative hydrodynamic heat transport away from the conventional heat diffusion. Fig. 1c shows the propagation of the hydrodynamic wave packet, characterized by diminishing intensity and broadening width. The moving wave pack demonstrates typical characteristics of fluid. The inset of Fig. 1c represents the decay of the wave intensity, fitted by dual exponential terms, suggesting the decay of the wave packet involves two processes. The timescale of the rapid process is comparable to the phonon lifetime, thus, during this process, phonons experience insufficient scatterings and transport ballistically analogy to radiation. The rapid process fades within 1 ns, indicating that ballistic component is negligible at the time points shown in Fig. 1b. During the slow process, despite adequate scatterings occurring among the phonons within the wave packet, the wave packet still propagates collectively due to momentum-conserving Normal scatterings. From the slow process, we extract the propagation length l_p of the hydrodynamic wave shown in the inset of Fig. 1c.

3.3. Window of hydrodynamics transport

Utilizing *ab initio* Monte Carlo simulation, we are able to identify the length scale and temperature where the hydrodynamic phonon transport can be observed. At the scale far larger than l_p , the hydrodynamic waves extinct, leading to thermal transport governed by diffusion of phonons. When reducing the scale to phonon mean free path, the phonons travel ballistically and no longer support the continuity condition for hydrodynamic process. Therefore, the propagation length l_p and ballistic limit l_b defines a window for hydrodynamic regime as shown in Fig. 1a and d. The ballistic limit can be estimated as mode-averaged phonon mean free path,

$$\bar{\Lambda} = \frac{\sum_{qs} C_{qs} \Lambda_{qs}}{\sum_{qs} C_{qs}}$$

(13)

where C_{qs} is the volumetric specific heat and $\Lambda_{qs} = |\mathbf{v}_{qs}| \tau_{qs}$ is the phonon mean free path of the phonon mode qs . The calculated window for hydrodynamic phonon transport is shown in Fig. 1d. From Fig. 1d, the hydrodynamic process exists in isotopically pure graphite up to 250 K at the length around 0.14 μm .

3.4. Quantified strong normal scatterings in Graphite

The hydrodynamic phonon transport is caused by strong Normal scatterings compared with Umklapp scatterings. As shown in Fig. 2a, the Normal scatterings can strictly conserve the momentum of phonons defined as $\hbar\mathbf{q}$, while the Umklapp scatterings cannot. Since the phonon wavelength are always longer than the lattice parameters, the phonon wave vectors should always stay inside the Γ -centered first Brillouin Zone. Once a phonon scattering process generates a phonon mode out of the first Brillouin Zone, the phonon wave vector will be transformed back to the first Brillouin Zone based on translational invariance as shown in Fig. 2a, which as a result destroys the phonon momentum. Strong Umklapp scatterings could prevent a large deviation from equilibrium distribution, keep the average phonon velocity near zero, and avoid convective phonon transport. On the other hand, the Normal scatterings can maintain the momentum of the phonon flux, which makes the phonon flows behave like fluid.

To quantitatively verify the strong Normal scattering in graphite, we demonstrate the ratio of normal scattering rates τ_N^{-1} to total scattering rates τ_{total}^{-1} at 100 K at $\mathbf{q}_z = 0$ plane for the selected phonon branches in Fig. 2b, indicating vast majority of the phonon modes are dominated by normal scatterings. In the flexural acoustic (ZA), transverse acoustic (TA), longitudinal acoustic (LA), and first flexural optical (ZO1) branches presented in Fig. 2b, around 84% of the phonon modes exhibit Normal scattering rates surpassing Umklapp scattering rates. In the remaining 8 optical branches which are occupied by only 5% of the phonons, half of the phonon modes still present Normal scattering rates exceeding Umklapp scattering rates. The strong Normal scattering in Graphite is the reason of the observed hydrodynamic phonon transport.

3.5. Hydrodynamic phonon vortex

As a further step, we simulate the phonon transport in hydrodynamic regime and compared with the transport features derived from heat diffusion model and fluid model (see Appendix B). The heat diffusion equations and fluid equations are solved by finite element methods using COMSOL Multiphysics [39]. We observed convective features in solid heat conduction due to hydrodynamic phonon transport.

In Fig. 3a–c, heat transport in a 1- μm -wide square disk at a background temperature of 100 K is simulated using the phonon BTE and compared with results from the heat diffusion and fluid model. In the heat diffusion model and phonon BTE, a 0.2- μm -width heating source and cooling source are positioned at the top edge of the left boundary and the right edge of the bottom boundary, respectively. In the fluid model, the heating and cooling sources are replaced with fluid inlet and outlet. The insulative, slip, and specular boundary conditions

are applied in the heat diffusion model, fluid model, and phonon BTE, respectively. Fig. 3a–c shows the resultant flux fields with streamlines. Fig. 3a demonstrates the absence of vortex in heat flux as calculated by heat diffusion model, since the vortex cannot be generated through diffusion processes. Fig. 3b shows a vortex at the corner by fluid model, as indicated by the streamlines. In Fig. 3c, the phonon flux by BTE also demonstrates a vortex at the corner, which illustrates the convective feature in solid heat conduction due to the hydrodynamic phonon transport.

To explore the formation conditions of the phonon vortex, we investigate the effects of disk size and background temperature in Fig. 3d and e, respectively. In Fig. 3d, we compute the heat flux fields for square widths ranging from 50 nm to 7.5 μm , maintaining a fixed flux density at the heating and cooling sources and a constant background equilibrium temperature. We observe that as the width of the square increases from 1 μm to 3 μm , the vortex at the top right corner disappears. Regarding the vortex at the bottom left corner, its size grows from approximately 0.5 μm to around 1.2 μm when the width of the square extends from 1 μm to 3 μm , and remains constant as the square width further increases to 5 μm . At 1 μm width, the size of the vortex is limited by the dimensions of the square disk. As the square width expands, the size of the vortex is no longer constrained by the geometry and becomes comparable with the average phonon mean free path. When the width of the square further increases to 7.5 μm , the phonon vortex disappears as the phonon density wave originating from the heating source cannot propagate a sufficiently long distance to form a vortex in such a large disk. Consequently, at a width of 7.5 μm , thermal transport transits from convective to diffusive. On the other hand, as the size of the disk decreases, the streamlines gradually become increasingly tortuous. At 100 nm width, the vortex at the top right corner splits into two. Furthermore, at 50 nm width, phonons travel ballistically without sufficient scatterings since the size of the disk becomes less than the phonon mean free path, leading the flux field and streamline to appear more chaotic due to the anisotropic nature of the crystal along various orientations. In Fig. 3e, we compute the heat flux field under varying background equilibrium temperature, while fixing the geometry. As the temperature increases, the thermal transport transit from convective to diffusive due to the reduced propagation length of phonon density wave. At 150 K, the vortex at top right corner disappears, and at 200 K, the vortex at bottom left corner vanishes. In contrast, with the decrease of temperature, the thermal transport transit from convective to ballistic due to increased phonon mean free path. At 50 K, the flux field and streamline exhibit chaotic and tortuous patterns. Based our study, we found that the convective phonon transport occurs within a specific range of size and temperature. At lower temperatures or smaller sizes, when the phonon mean free path exceeds the size of the domain, the thermal transport becomes ballistic. On the other hand, at higher temperatures or larger sizes, when the propagation length of phonon density wave is shorter than the size of the domain, the thermal transport becomes diffusive.

3.6. Hydrodynamic phonon jet

To further explore the characteristics of hydrodynamic phonon transport, we use *ab initio* Monte Carlo simulations to demonstrate the formation of a phonon jet flow arising from the propagation of phonon wave packets in hydrodynamic regime. In Fig. 4a–c, we simulate

the transport process of the jet flow at 100 K, originating from a 0.2- μm -width inlet or heat source. In the heat diffusion model, we apply thermal insulation boundary condition at left and side boundaries, and fixed temperature boundary condition at right boundary. In the fluid model, we apply no-slip, slip, and open boundary condition for left, side, and right boundaries, respectively. In phonon BTE, we apply diffusive, specular, and equilibrium temperature boundary condition for left, side, and right boundaries, respectively. The simulation domain is sufficiently large to ensure negligible effects from the side and right boundaries on the demonstrated region. In a heat diffusion process, as shown in Fig. 4a, the isocontour of the flux density shows a semicircle shape, reflecting the uniform distribution of flux density from a point heater over various angles. While for fluid in Fig. 4b, the jet flow is highly directional due to the bulk motion of the fluid. Similarly, in Fig. 4c, the heat flux field by phonon BTE also demonstrates a strong directional characteristic, illustrating fluid-like features in solid heat transfer due to phonon convection. Our simulations in real geometries uncover the fluid-like convective features of heat conduction in solids.

To comprehensively understand the behavior of the phonon jet flow, we examined the impact of inlet width and background temperature based on phonon BTE in Fig. 4d and e, respectively. As both the inlet width and temperature decrease, the phonon jet flow becomes more directional due to longer phonon mean free path relative to the characteristic length of the thermal transport. Conversely, as the inlet width and temperature rise, the phonon jet flow gradually become less directional and approaches to diffusive transport due to the increased phonon scatterings that diminish the directional nature of the flow.

4. Conclusion

In summary, we investigate the convection of phonons in heat conduction processes based on *ab initio* approaches. The hydrodynamic phonon transport is simulated by solving the phonon BTE with the scattering matrix determined by quantum perturbation theory using *ab initio* approaches based on density functional theory. The fluid-like features such as vortex and jet flow are captured by the BTE beyond relaxation time approximation and compared with the heat diffusion model based on Fourier's law and the fluid model based on Navier-Stokes equation. We observed the fluid-like convective features in heat conduction that was missed in classical heat transfer theory. This work expands the fundamental understandings of the heat conduction from quantum theory and atomistic scale simulations. The investigations on the phonon convection could innovate the thermal design of the future microelectronic industries [26,40,41] and other thermal management applications [42–44], which potentially opens opportunities to address the heat dissipation issues in the post-Moore era.

Acknowledgement

Y.H. acknowledges support from a NIGMS Research Award under Grant No. R35GM147391, a NSF Grant DMR-1753393, and Alfred P. Sloan Research Fellowship under Grant No. FG-2019-11788. This work used computational and storage services associated with the Hoffman2 Shared Cluster provided by UCLA Office of Advanced Research Computing's Research Technology Group, and the Bridges-2 at Pittsburgh Supercomputing Center through allocation DMR180111 from Extreme Science and Engineering Discovery Environment which was supported by National Science Foundation grant number 1548562, and the Bridges-2 at Pittsburgh Supercomputing Center through allocation DMR180111 from the Advanced Cyberinfrastructure Coordination Ecosystem: Services

& Support program which was supported by National Science Foundation grant number 2138259, 2138286, 2138307, 2137603, and 2138296.

Data availability

Data will be made available on request.

Appendix A

To fully validate our numerical procedure, we compared our calculated size-dependent nanowire thermal conductivity with the semi-analytical approximate solutions [45]. Under temperature gradient ∇T , the phonon distribution (n_{qs}) deviates from equilibrium Bose-Einstein distribution (n_{qs}^0), and can be expanded as

$$n_{qs} = n_{qs}^0 - \frac{\partial n_{qs}^0}{\partial T} F_{qs} \cdot \nabla T \quad (\text{A1})$$

where qs denotes a phonon mode with wavevector \mathbf{q} and polarization s , and F_{qs} is the expansion coefficient that quantifies the deviation of phonon distribution. Given that the cross-plane phonon mean free path is shorter than the width of the nanowire, while the in-plane phonon mean free path exceeds the width, we assume that confinement occurs only in the in-plane direction. By solving Boltzmann transport equation with relaxation time approximation, $F_{qs}(y)$ varies with the distance to boundary y , and can be approximately expressed as

$$F_{qs}(y) = \begin{cases} F_{qs}^\infty \left[1 - \exp\left(-\frac{y}{\Lambda_{y,qs}}\right) \right], & 0 < y \leq \frac{W}{2} \\ F_{qs}^\infty \left[1 - \exp\left(-\frac{W-y}{\Lambda_{y,qs}}\right) \right], & \frac{W}{2} < y \leq W \end{cases} \quad (\text{A2})$$

where W is the width of the nanowire, and $\Lambda_{y,qs} = |\mathbf{v}_{y,qs}| \tau_{qs}$ is the in-plane phonon mean free path. Here, a diffusive boundary condition is applied, assuming phonons are fully equilibrium at the boundary, i.e., $F_{qs}(y=0) = 0$. F_{qs}^∞ is the F_{qs} in bulk materials and can be obtained by solving Boltzmann transport equation through self-consistent iterations [15].

When applying ∇T along the nanowire, the heat flux J is given by

$J = \int_S \frac{1}{N} \sum_{qs} \hbar \omega_{qs} \mathbf{v}_{qs}^\alpha (n_{qs}(y) - n_{qs}^0) ds = -S \kappa \nabla T$, where S denotes the cross-sectional area and α represents the projection along nanowire. From this, the thermal conductivity of nanowire, κ , can be subsequently derived as

$$\kappa = \frac{1}{N} \sum_{qs} C_{qs} \mathbf{v}_{qs}^\alpha \bar{F}_{qs}^\alpha \quad (\text{A3})$$

where \bar{F}_{qs}^α is cross-section average of $F_{qs}^\alpha(y)$,

$$\bar{F}_{qs}^\alpha = F_{qs}^{\infty, \alpha} \left\{ 1 - \frac{4\Lambda_{qs}}{W} \left[1 - \exp\left(-\frac{W}{4\Lambda_{y,qs}}\right) \right] \right\} \quad (\text{A4})$$

In Fig. 5, we compared the *ab initio* Monte Carlo results with semi-analytical approximate solution, focusing on graphite nanowire along the armchair orientation. The agreement shown in Fig. 5 validates our numerical approach. At $W = 0.1 \mu\text{m}$, the semi-analytical solution slightly over-estimates the thermal conductivity due to the neglect of confinement in the cross-plane direction. At $W > 0.5 \mu\text{m}$, semi-analytical solution slightly underestimates the thermal conductivity due the implication of relaxation time approximation.

Appendix B

In fluid model, we consider a steady-state laminar flow. The equation set is as follows,

$$\rho \nabla \cdot \mathbf{u} = 0 \quad (\text{B1})$$

$$\rho(\mathbf{u} \cdot \nabla)\mathbf{u} = \nabla \cdot \left(-p\mathbf{I} + \mu(\nabla\mathbf{u} + (\nabla\mathbf{u})^T) \right) \quad (\text{B2})$$

where Eq. (B1) and Eq. (B2) are the continuity equation and Navier-Stokes momentum equation, respectively. \mathbf{u} is velocity. ρ and μ are density and dynamic viscosity, respectively. In Fig. 3c, a pressure difference at 10 kPa is applied between inlet and outlet. In Fig. 4c, the inlet velocity is set to be 15 m/s.

References

- [1]. Incropera FP, DeWitt DP, Bergman TL, Lavine AS, Fundamentals of Heat and Mass Transfer, 8th Edition, Wiley, 2017.
- [2]. Ziman JM, Electrons and Phonons: The Theory of Transport Phenomena in Solids, Oxford University Press, Oxford, 1960.
- [3]. Prohofsky EW, Krumhansl JA, Second-sound propagation in dielectric solids, Phys. Rev. 133 (1964) A1403.
- [4]. Hardy RJ, Phonon Boltzmann equation and second sound in solids, Phys. Rev. B 2 (1970) 1193.
- [5]. Cepellotti A, Fugallo G, Paulatto L, Lazzeri M, Mauri F, Marzari N, Phonon hydrodynamics in two-dimensional materials, Nat. Commun. 6 (2015) 6400. [PubMed: 25744932]
- [6]. Lee S, Broido D, Esfarjani K, Chen G, Hydrodynamic phonon transport in suspended graphene, Nat. Commun. 6 (2015) 6290. [PubMed: 25693180]
- [7]. Ward JC, Wilks J III, Second sound and the thermo-mechanical effect at very low temperatures, Lond. Edinbur. Dublin Philos. Mag. J. Sci. 43 (1952) 48–50.
- [8]. Guo Y, Wang M, Phonon hydrodynamics and its applications in nanoscale heat transport, Phys. Rep. 595 (2015) 1–44.

- [9]. Ward A, Broide DA, Stewart DA, Deinzer G, Ab Initio theory of the lattice thermal conductivity in diamond, *Phys. Rev. B* 80 (2009), 125203.
- [10]. Esfarjani K, Chen G, Stokes HT, Heat transport in silicon from first-principles calculations, *Phys. Rev. B* 84 (2011), 085204.
- [11]. Garg J, Bonini N, Kozinsky B, Marzari N, Role of disorder and anharmonicity in the thermal conductivity of silicon-germanium alloys: a first-principles study, *Phys. Rev. Lett.* 106 (2011), 045901. [PubMed: 21405336]
- [12]. Feng T, Ruan X, Quantum mechanical prediction of four-phonon scattering rates and reduced thermal conductivity of solids, *Phys. Rev. B* 93 (2016), 045202.
- [13]. Kang JS, Li M, Wu H, Nguyen D, Hu Y, Experimental observation of high thermal conductivity in boron arsenide, *Science* 361 (2018) 575–578. [PubMed: 29976798]
- [14]. Fan H, Wu H, Lindsay L, Hu Y, Ab Initio investigation of single-layer high thermal conductivity boron compounds, *Phys. Rev. B* 100 (2019), 085420.
- [15]. Wu H, Fan H, Hu Y, Ab Initio determination of ultrahigh thermal conductivity in ternary compounds, *Phys. Rev. B* 103 (2021), L041203.
- [16]. Li S, Qin Z, Wu H, Li M, Kunz M, Alatas A, Kavner A, Hu Y, Anomalous thermal transport under high pressure in boron arsenide, *Nature* 612 (2022) 459–464. [PubMed: 36418403]
- [17]. Wu H, Qin Z, Li S, Lindsay L, Hu Y, Nonperturbative determination of isotope-induced anomalous vibrational physics, *Phys. Rev. B* 108 (2023), L140302. [PubMed: 38881566]
- [18]. Callaway J, Model for lattice thermal conductivity at low temperatures, *Phys. Rev.* 113 (1959) 1046.
- [19]. Li X, Lee S, Role of hydrodynamic viscosity on phonon transport in suspended graphene, *Phys. Rev. B* 97 (2018) 94309.
- [20]. Li X, Lee S, Crossover of ballistic, hydrodynamic, and diffusive phonon transport in suspended graphene, *Phys. Rev. B* 99 (2019) 85202.
- [21]. Jeong J, Li X, Lee S, Shi L, Wang Y, Transient hydrodynamic lattice cooling by picosecond laser irradiation of graphite, *Phys. Rev. Lett.* 127 (2021) 85901.
- [22]. Huberman S, Duncan RA, Chen K, Song B, Chiloyan V, Ding Z, Maznev AA, Chen G, Nelson KA, Observation of second sound in graphite at temperatures above 100K, *Science* 364 (2019) 375–379. [PubMed: 30872535]
- [23]. Shang MY, Zhang C, Guo Z, Lü JT, Heat vortex in hydrodynamic phonon transport of two-dimensional materials, *Sci. Rep.* 10 (2020) 8272. [PubMed: 32427969]
- [24]. Guo Y, Zhang Z, Nomura M, Volz S, Wang M, Phonon vortex dynamics in graphene ribbon by solving Boltzmann transport equation with Ab Initio scattering rates, *Int. J. Heat Mass Transf.* 169 (2021), 120981.
- [25]. Kang JS, Wu H, Hu Y, Thermal properties and phonon spectral characterization of synthetic boron phosphide for high thermal conductivity applications, *Nano Lett* 17 (2017) 7507–7514. [PubMed: 29115845]
- [26]. Kang JS, Li M, Wu H, Nguyen H, Aoki T, Hu Y, Integration of boron arsenide cooling substrates into gallium nitride devices, *Nat. Electron.* 4 (2021) 416.
- [27]. Landon CD, Hadjiconstantinou NG, Deviation simulation of phonon transport in graphene ribbons with Ab initio scattering, *J. Appl. Phys.* 116 (2014), 163502.
- [28]. Srivastava GP, *The Physics of Phonons*, CRC Press, 1990.
- [29]. Hohenberg P, Kohn W, Inhomogeneous Electron Gas, *Phys. Rev.* 136 (1964) B864.
- [30]. Kohn W, Sham LJ, Self-consistent equations including exchange and correlation effects, *Phys. Rev.* 140 (1965) A1133.
- [31]. Giannozzi P, et al. , QUANTUM ESPRESSO: a modular and open-source software project for quantum simulations of materials, *J. Phys.: Condens. Matter* 21 (2009), 395502. [PubMed: 21832390]
- [32]. Giannozzi P, et al. , Advanced capabilities for materials modelling with quantum ESPRESSO, *J. Phys.: Condens. Matter* 29 (2017), 465901. [PubMed: 29064822]

- [33]. Tadano T, Gohda Y, Tsuneyuki S, Anharmonic force constants extracted from first-principles molecular dynamics: applications to heat transfer Simulations, *J. Phys.: Condens. Matter* 26 (2014), 225402. [PubMed: 24824156]
- [34]. Klimeš J, Bowler DR, Michaelides A, Van Der waals density functionals applied to solids, *Phys. Rev. B* 83 (2011), 195131.
- [35]. Péraud JPM, Hadjiconstantinou NG, Efficient simulation of multidimensional phonon transport using energy-based variance-reduced Monte Carlo formulations, *Phys. Rev. B* 84 (2011), 205331.
- [36]. Peterson RB, Direct simulation of phonon-mediated heat transfer in a debye crystal, *J. Heat Transfer* 116 (4) (1994) 815–822.
- [37]. Mazumder S, Majumdar A, Monte Carlo study of phonon transport in solid thin films including dispersion and polarization, *J. Heat Transfer* 123 (4) (2001) 749–759.
- [38]. Hao Q, Chen G, Jeng MS, Frequency-dependent Monte Carlo simulations of phonon transport in two-dimensional porous silicon with aligned pores, *J. Appl. Phys.* 106 (2009), 114321.
- [39]. COMSOL Inc., COMSOL multiphysics, v6.0.
- [40]. Cui Y, Li M, Hu Y, Emerging interface materials for electronics thermal management: experiments, modeling, and new opportunities, *J. Mater. Chem. C* 8 (2020) 10568–10586.
- [41]. Cui Y, Qin Z, Wu H, Li M, Hu Y, Flexible thermal interface based on self-assembled boron arsenide for high-performance thermal management, *Nat. Commun.* 12 (2021) 1284. [PubMed: 33627644]
- [42]. Qin Z, Li M, Flohn J, Hu Y, Thermal management materials for energy-efficient and sustainable future buildings, *Chem. Commun.* 57 (2021) 12236–12253.
- [43]. Li M, Dai L, Hu Y, Machine learning for harnessing thermal energy: from materials discovery to system optimization, *ACS Energy Lett* 7 (2022) 3204–3226. [PubMed: 37325775]
- [44]. Li M, Wu H, Avery EM, Qin Z, Goronzy DP, Nguyen H, et al. , Electrically gated molecular thermal switch, *Science* 382 (2023) 585–589. [PubMed: 37917706]
- [45]. Chambers RG, The conductivity of thin wires in a magnetic field, *Proc. R. Soc. Lond. A* 202 (1950) 378–394.

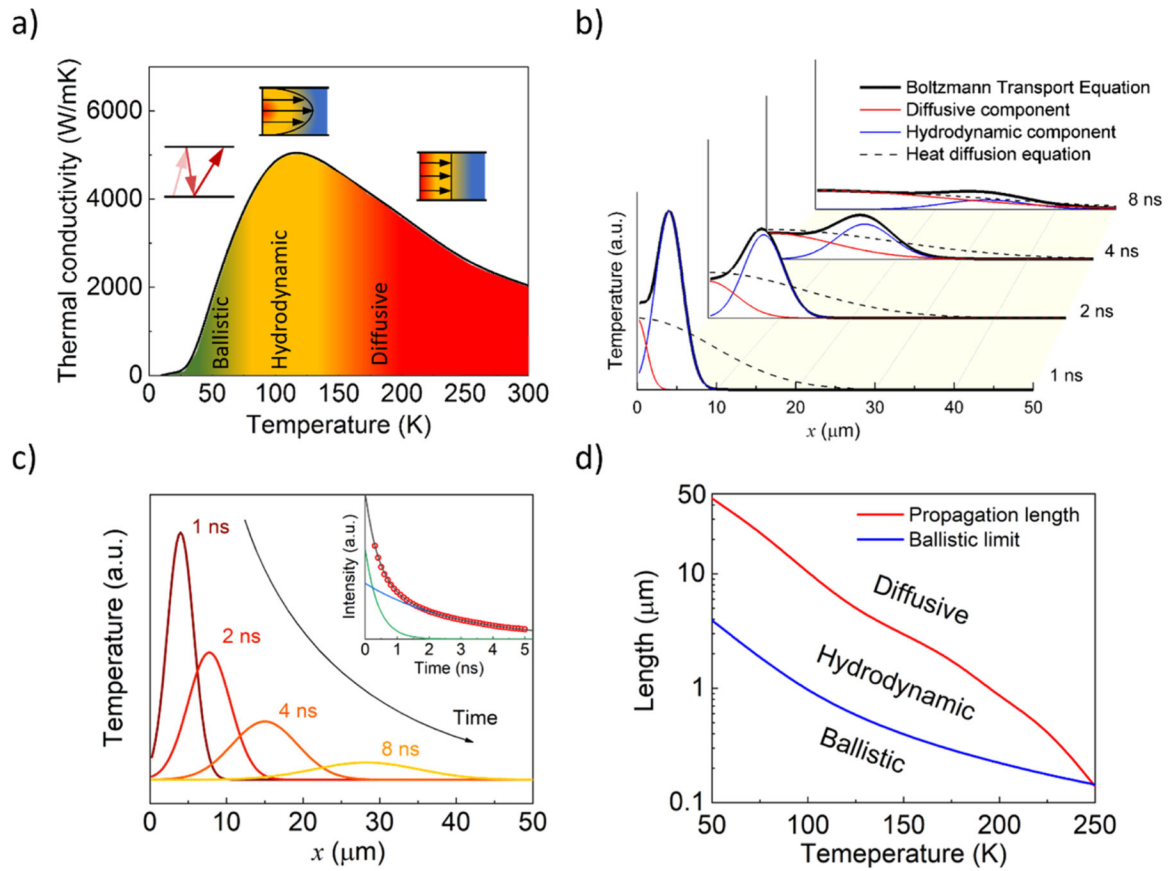


Fig. 1. *Ab initio* analysis of hydrodynamic phonon transport in isotopically pure graphite.

a) Thermal conductivity of 4- μm -width graphite nanowire in ballistic, hydrodynamic, and diffusive regimes as a function of temperature. b) Temperature field response to a heat pulse under a background temperature of 100 K. The temperature field determined by the phonon Boltzmann transport equation (black solid) is a superposition of the diffusive (red solid) and hydrodynamic (blue solid) components, and shows noticeable difference from the heat diffusion equation solution (black dashed). c) Visualization of hydrodynamic wave pack propagation. The inset shows the fitting of the slow and fast processes occurring during the intensity decay of the temperature wave. d) Window for hydrodynamic phonon transport.

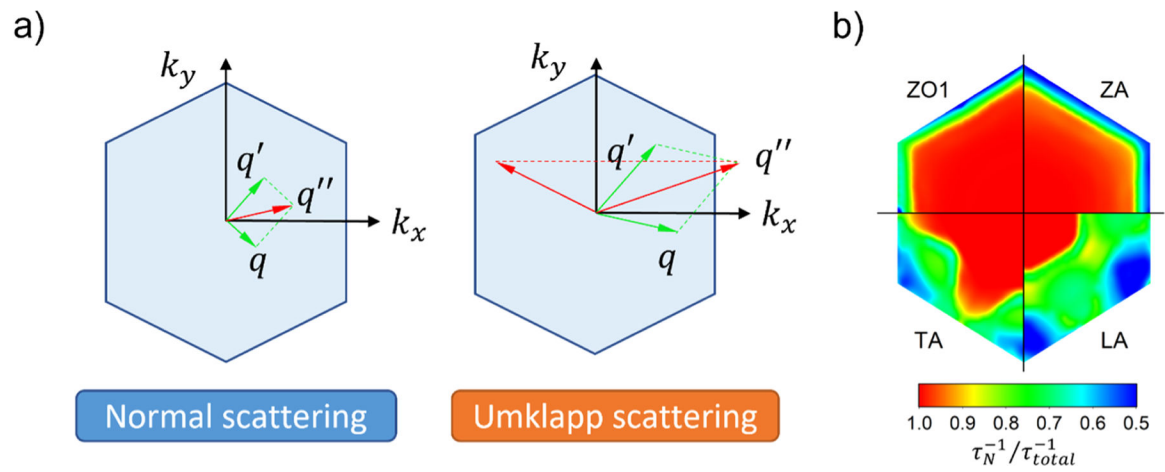


Fig. 2. Intrinsic phonon spectral properties that lead to strong phonon hydrodynamic.

a) Schematic of Normal scattering and Umklapp scattering. b) Portion of Normal scatterings at $q_z = 0$ for selected phonon branches, including flexural acoustic (ZA), transverse acoustic (TA), longitudinal acoustic (LA), and first flexural optical (ZO1) branches.

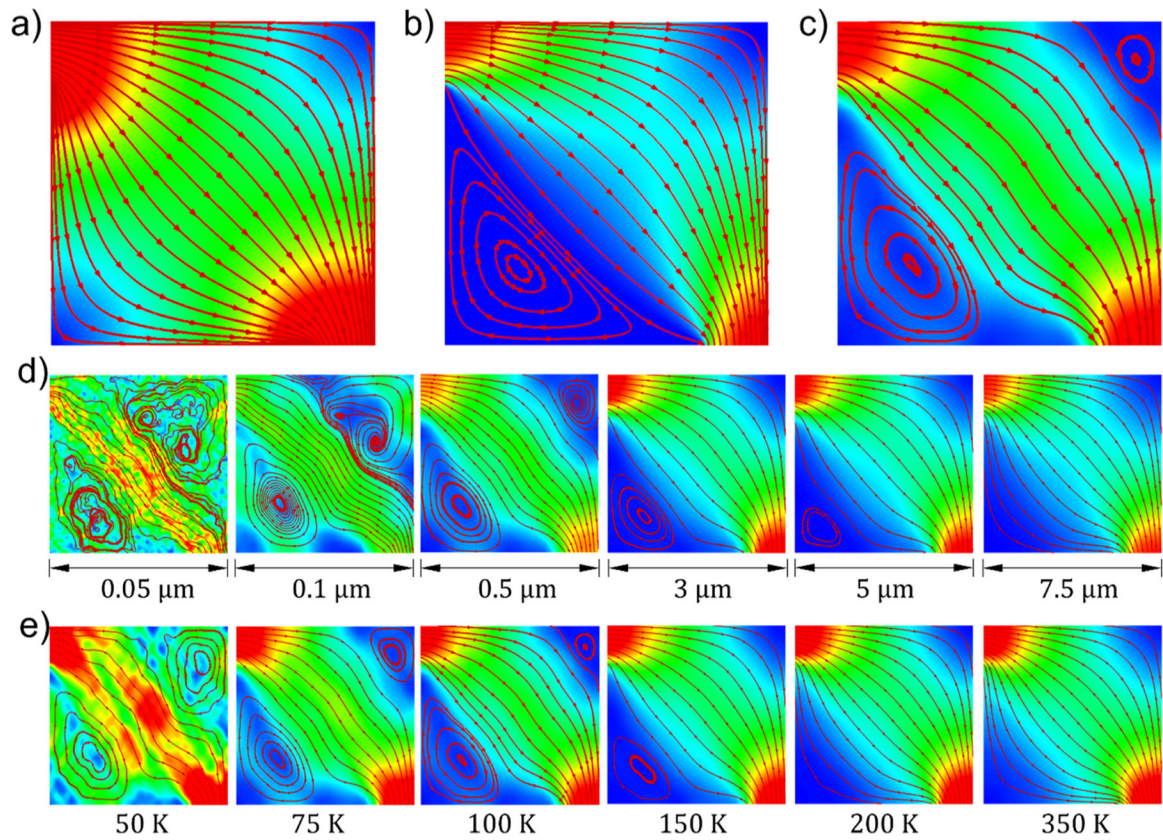


Fig. 3. Flux fields and streamlines of vortex generated at the corner of a square disk.

(a-c) Comparison in a 1- μm -width square disk at 100 K among (a) heat diffusion model, (b) fluid model, and (c) Boltzmann transport equations with *ab initio* phonon interactions. (d) Compare the effects of varying disk size under a fixed background temperature at 100 K. (e) Compare the effects of varying background temperature with fixed disk width at 1 μm . Both (d) and (e) are derived from Boltzmann transport equations with *ab initio* phonon interactions. The colormap represents the magnitude of flux density, the red curve shows the streamlines, and the red arrow indicates the flow direction.

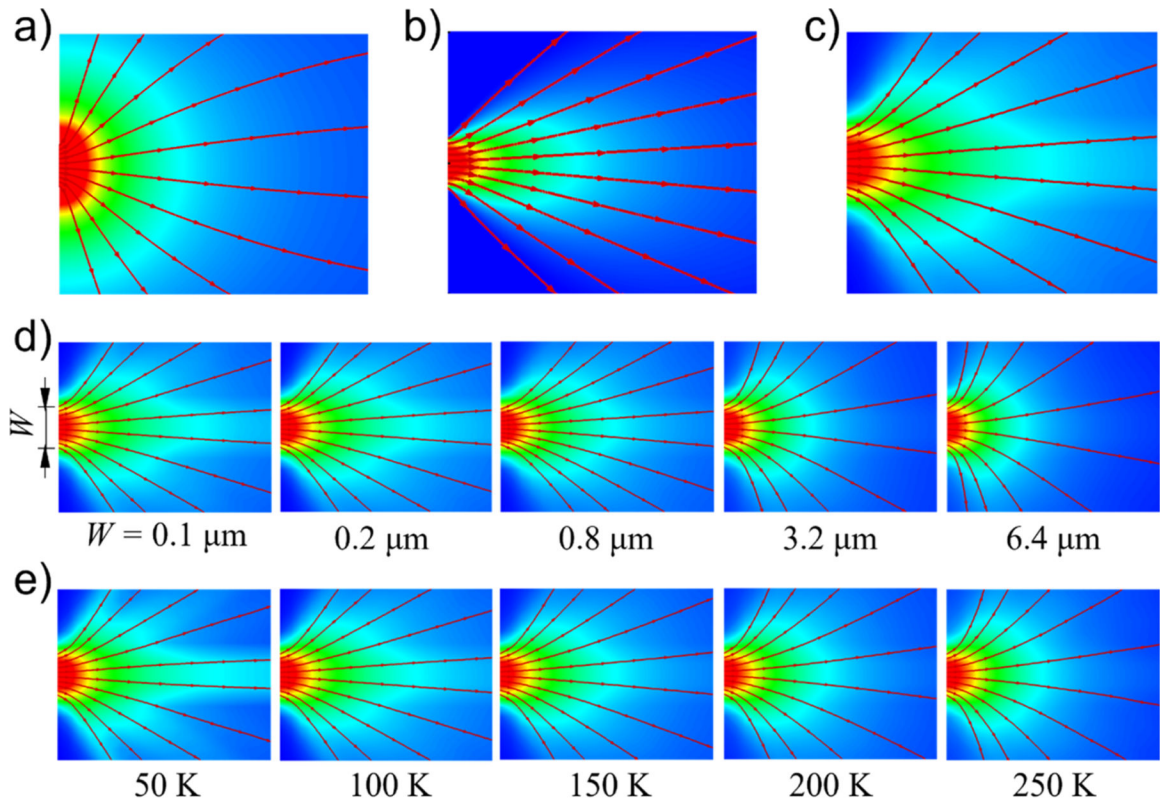


Fig. 4. Flux fields and streamlines of a jet flow.

(a-c) Comparison in a jet flow at 100 K originating from a 0.2- μm -width inlet among (a) heat diffusion model, (b) fluid model, and (c) Boltzmann transport equations with *ab initio* phonon interactions. (d) Compare the effects of varying inlet widths under a fixed background temperature at 100 K. (e) Compare the effects of varying background temperature with fixed inlet width at 0.2 μm . Both (d) and (e) are derived from Boltzmann transport equations with *ab initio* phonon interactions. The colormap represents the magnitude of flux density, the red curve shows the streamlines, and the red arrow indicates the flow direction.

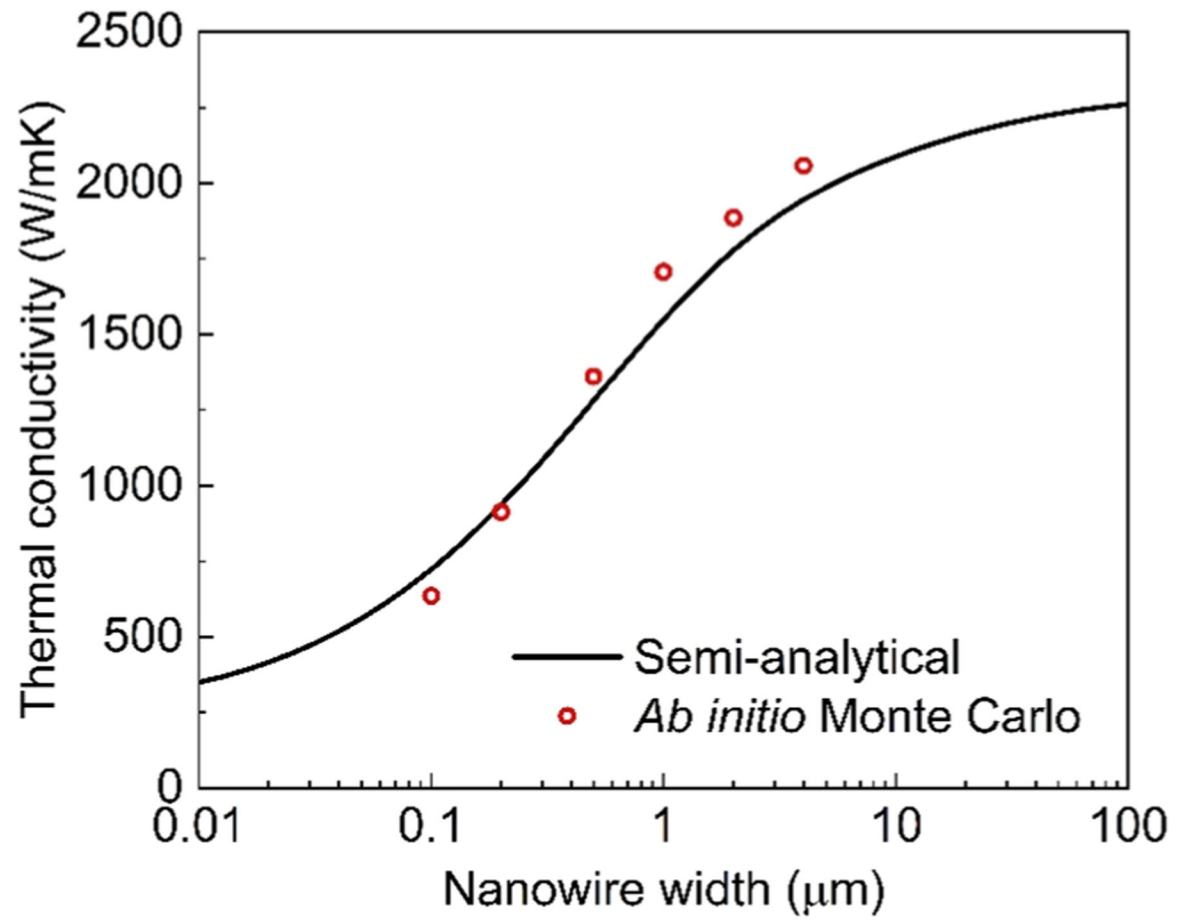


Fig. 5. Comparison between *ab initio* Monte Carlo results and semi-analytical approximate solution.